

Miniaturization of holographic Fourier-transform spectrometers

Nikolay I. Agladze and Albert J. Sievers

Wave propagation equations in the stationary-phase approximation have been used to identify the theoretical bounds of a miniature holographic Fourier-transform spectrometer (HFTS). It is demonstrated that the HFTS throughput can be larger than for a scanning Fourier-transform spectrometer. Given room- or a higher-temperature constraint, a small HFTS has the potential to outperform a small multichannel dispersive spectrograph with the same resolving power because of the size dependence of the signal-to-noise ratio. These predictions are used to analyze the performance of a miniature HFTS made from simple optical components covering a broad spectral range from the UV to the near IR. The importance of specific primary aberrations in limiting the HFTS performance has been both identified and verified. © 2004 Optical Society of America

OCIS codes: 220.1010, 220.4830, 260.3160, 300.6300.

1. Introduction

The first demonstration of a completely static Fourier-transform spectrometer (FTS) appeared in 1965.¹ A few other examples of a holographic FTS (HFTS) with optical transformation of the interferogram appeared somewhat later with a tilted mirror used in a Michelson–Twyman–Green interferometer,² a shearing Sagnac interferometer,³ a Lloyd's mirror,⁴ and a modified Mach–Zehnder interferometer.⁵ But rapid progress of digital computing power, the invention of the Cooley–Tukey algorithm,⁶ and cooled bolometric detectors permitted the Fellgett multiplex advantage^{7–10} to be realized. These developments firmly established practical step-scan and scanning FTSs, first in the far IR^{11–13} and later in the IR.¹⁴ Grating spectrometers still dominated the UV and visible region, where, because of the predominant photon noise, the Fellgett advantage is absent.

HFTS development resurfaced when the static interference pattern in the output of the interferometer could be sampled with a multichannel photodiode detector, connected to a microcomputer.^{15–23} The capability to provide imaging information in one direc-

tion with spectral information in the other, combined with a compact and rugged design with no moving parts, has made the HFTS attractive for remote sensing^{22,24} (often called a digital array scanned interferometer). To date the HFTS has been successfully tested in astronomy,¹⁹ single-event rapid spectroscopy,²⁵ Raman spectroscopy,²¹ and toxic gases monitoring.²⁶

Another emerging area where a HFTS should have a large potential is in spectral device miniaturization. Miniature dispersive spectrometers of a few centimeters in size are already available commercially.^{27,28} However, because of the large throughput of HFTS, an important question is whether it can be made significantly smaller than a corresponding multichannel dispersive type for a given resolving power. In this paper our theoretical and experimental efforts to shrink the size of the HFTS down to a chip-scale device are described.

In Section 2 the mathematical framework for the miniature HFTS operation is developed for the diffraction regime. The point eikonal function technique is used within the framework of the scalar stationary-phase approximation for approximately axially symmetric optics so that the intensity distribution across an array detector can be obtained in a general way. This method provides a rigorous derivation of the standard Fourier-transform result previously obtained for a HFTS with a simplified approach.^{15,29} An important new feature is the dependence of the signal-to-noise ratio on the size of the array detector, which is directly connected to the size

N. I. Agladze (agladze@ccmr.cornell.edu) and A. J. Sievers are with the Laboratory of Atomic and Solid State Physics, Cornell University, Ithaca, New York 14853-2501.

Received 8 July 2004; revised manuscript received 13 September 2004; accepted 18 September 2004.

0003-6935/04/366568-12\$15.00/0

© 2004 Optical Society of America

of the instrument. In Section 3 a miniature HFTS made from standard optical components is described. Its construction, operation, and testing are presented and the theoretical and experimental results are compared. The demonstrated resolving power and throughput produce a larger signal-to-noise ratio than is achievable with a competing miniature multichannel dispersive spectrometer. In Section 4 the performance-limiting effects due to monochromatic aberrations are simply related to phase shifts in the interferogram, which can be experimentally measured. Our findings are that astigmatism is more important than spherical aberration and that chromatic aberration results mainly in a spectral frequency shift, which can be readily corrected digitally.

2. Diffraction Theory of Holographic Fourier-Transform Spectrometer Operation

With the HFTS, we use a static interference pattern created by two coherent wave fronts. For an incoherent extended source, the wave fronts are split into two components and then recombined at the array detector. Among the many possible ways of doing this, transverse shearing of the source images (without flipping) results in the largest field of view and the highest throughput. Currently two main methods are used for wave-front shearing. One is based on birefringence^{21,23} and the other is used with beam splitters.^{15–19,22} The latter method is the subject of the present study.

A. Intensity Distribution at the Detector

The operation of a HFTS has already been described in which the interference between two wave fronts was considered with the help of a geometric construction with optical rays.²⁹ Here we derive the intensity distribution at the detector in a more general way by using the eikonal formalism and the scalar wave propagation equations in a stationary-phase approximation so that the intensity distribution across an array detector can be obtained for a large variety of input wave fronts with diffraction effects included.³⁰

Schematically, the optical system of a HFTS can be represented as an object (an arbitrary superposition of the field amplitudes) in the front focal plane (field of view in the optical design literature) of a Fourier lens, whereas the detector coincides with the back focal plane of that lens. This representation is shown in Fig. 1 where f is the focal length of the lens in vacuum, so that in the object space it is nf and in the image space it is $n'f$, where n and n' are the corresponding indices of refraction. Let $S(x, y, x', y')$ be a point eikonal between the reference planes located at the front and back focal positions of the lens F . The positions of points P and P' in the reference planes in Fig. 1 can be described by two-dimensional vectors $\mathbf{r}(x, y)$ and $\mathbf{r}'(x', y')$, respectively, where in accordance with standard optical design practice the vertical (meridional) direction corresponds to the Y axis whereas the Z and Z' axes are directed from left to right and coincide with the optical axis. The shearing interferometer (not shown in the Fig. 1)

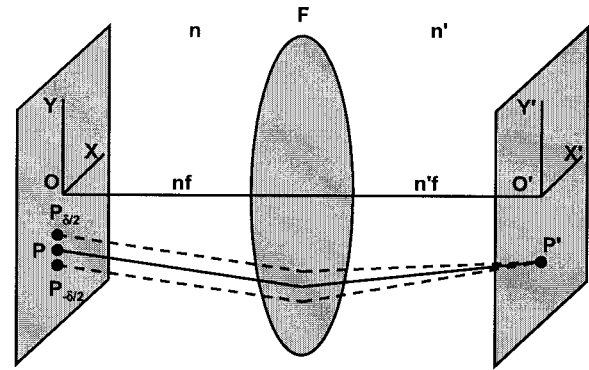


Fig. 1. Schematic illustration of the HFTS operation. Reference planes are perpendicular to the optical axis and pass through the front (object plane or field) and back (detector plane) foci of the Fourier lens F . Shearing in the interferometer is described as splitting of an arbitrary object point P by vectors $\pm \delta/2$ along the Y axis. Object and image reference planes have corresponding coordinate systems with vertical axes Y and Y' (meridional direction) and horizontal axes X and X' (sagittal direction). The Z and Z' axes (not shown) are both directed from the left to right and coincide with the optical axis.

replaces point P with two new virtual points with coordinates $(x, y + \delta/2)$ and $(x, y - \delta/2)$ or $\mathbf{r} + \delta/2$ and $\mathbf{r} - \delta/2$. As a result, the complex amplitude $U(\mathbf{r})$ in the object plane can be represented as a sum of two mutually coherent amplitudes shifted from the original position by a vector $\pm \delta/2$ so that

$$U(\mathbf{r}) \Rightarrow 1/2U(\mathbf{r} - \delta/2) + 1/2U(\mathbf{r} + \delta/2). \quad (1)$$

Here, for simplicity, an equal division of the amplitudes is assumed.

For an incoherent source the intensity at the detector is expressed as an average of the square modulus of the amplitude (see Ref. 30, p. 133) so that

$$\begin{aligned} I(\mathbf{r}') &= \langle |U'(\mathbf{r}')|^2 \rangle \\ &= \iint K_P^*(\mathbf{r}_1, \mathbf{r}') K_P(\mathbf{r}_2, \mathbf{r}') \langle U^*(\mathbf{r}_1) U(\mathbf{r}_2) \rangle d\mathbf{r}_1 d\mathbf{r}_2. \end{aligned} \quad (2)$$

In Eq. (2) the primed symbols represent variables in the image space, and the propagation kernel $K_P(\mathbf{r}, \mathbf{r}')$ in the stationary-phase approximation (see Ref. 30, p. 180) is

$$K_P(\mathbf{r}, \mathbf{r}') = \frac{n}{n'\lambda} \left(\frac{n'\mathcal{N}}{n\mathcal{N}'} \tau \right)^{1/2} |\text{Det}_{11} S|^{1/2} \exp ikS, \quad (3)$$

where

$$\text{Det}_{11} S \equiv \begin{vmatrix} \frac{\partial^2 S}{\partial x \partial x'} & \frac{\partial^2 S}{\partial x \partial y'} \\ \frac{\partial^2 S}{\partial y \partial x'} & \frac{\partial^2 S}{\partial y \partial y'} \end{vmatrix}.$$

Here λ is a wavelength in vacuum, $k = 2\pi/\lambda$ is the wave vector, τ is the device transmission, and \mathcal{N} and

N' are direction cosines of the rays with respect to the optical axis. The average in the integral in Eq. (2) is

$$\begin{aligned} \langle U^*(\mathbf{r}_1)U(\mathbf{r}_2) \rangle &= \frac{1}{4} \begin{bmatrix} \langle U^*(\mathbf{r}_1 - \delta/2)U(\mathbf{r}_2 - \delta/2) \rangle \\ + \langle U^*(\mathbf{r}_1 + \delta/2)U(\mathbf{r}_2 + \delta/2) \rangle \\ + \langle U^*(\mathbf{r}_1 - \delta/2)U(\mathbf{r}_2 + \delta/2) \rangle \\ + \langle U^*(\mathbf{r}_1 + \delta/2)U(\mathbf{r}_2 - \delta/2) \rangle \end{bmatrix} \\ &= \frac{1}{4} \begin{bmatrix} I(\mathbf{r}_1 - \delta/2)\delta(\mathbf{r}_1 - \mathbf{r}_2) \\ + I(\mathbf{r}_1 + \delta/2)\delta(\mathbf{r}_1 - \mathbf{r}_2) \\ + I(\mathbf{r}_1 - \delta/2)\delta(\mathbf{r}_1 - \mathbf{r}_2 - \delta) \\ + I(\mathbf{r}_1 + \delta/2)\delta(\mathbf{r}_1 - \mathbf{r}_2 + \delta) \end{bmatrix}, \end{aligned} \quad (4)$$

where the incoherent property of the source is given by the intensity relation

$$\langle U^*(\mathbf{r}_1)U(\mathbf{r}_2) \rangle = I(\mathbf{r}_1)\delta(\mathbf{r}_1 - \mathbf{r}_2). \quad (5)$$

We obtain the intensity at the detector by substituting Eq. (4) into Eq. (2):

$$\begin{aligned} I(\mathbf{r}') &= 1/4 \int |K_P(\mathbf{r} - \delta/2, \mathbf{r}') + K_P(\mathbf{r} \\ &\quad + \delta/2, \mathbf{r}')|^2 I(\mathbf{r})d^2\mathbf{r}. \end{aligned} \quad (6)$$

For a sufficiently small shift δ , the preexponential factor in Eq. (3) is unchanged, so the sum of the two kernels in Eq. (6) can be expressed through corresponding point eikonals as

$$\begin{aligned} &K_P(\mathbf{r} - \delta/2, \mathbf{r}') + K_P(\mathbf{r} + \delta/2, \mathbf{r}') \\ &= \frac{n}{n'\lambda} \left(\frac{n'\mathcal{N}}{n\mathcal{N}'\tau} \right)^{1/2} |\text{Det}_{11}S|^{1/2} [\exp ikS(\mathbf{r} - \delta/2, \mathbf{r}') \\ &\quad + \exp ikS(\mathbf{r} + \delta/2, \mathbf{r}')]. \end{aligned} \quad (7)$$

For an ideal Fourier lens the point eikonal (see Ref. 30, p. 184) reduces to

$$S_0(x, y, x', y') = -(xx' + yy')/f, \quad (8)$$

where the unimportant constant term ($nf + n'f$) was dropped. Substitution of Eq. (8) into Eq. (7) yields

$$\begin{aligned} &K_P(\mathbf{r} - \delta/2, \mathbf{r}') + K_P(\mathbf{r} + \delta/2, \mathbf{r}') \\ &= 2 \frac{n}{n'\lambda} \left(\frac{n'\mathcal{N}}{n\mathcal{N}'\tau} \right)^{1/2} |\text{Det}_{11}S|^{1/2} \exp ikS_0(\mathbf{r}, \mathbf{r}') \cos \frac{k\delta}{2f} y' \\ &= 2K_P(\mathbf{r}, \mathbf{r}') \cos \frac{k\delta}{2f} y'. \end{aligned} \quad (9)$$

Finally, substituting this expression into Eq. (6) produces the intensity at the array detector for a single monochromatic component, namely,

$$\begin{aligned} I(\mathbf{r}') &= 1/2 \left(1 + \cos \frac{k\delta}{f} y' \right) \int |K_P(\mathbf{r}, \mathbf{r}')|^2 I(\mathbf{r})d^2\mathbf{r} \\ &= 1/2 I_0(\mathbf{r}') \left(1 + \cos \frac{k\delta}{f} y' \right) \\ &= 1/2 I_0(\mathbf{r}') \left(1 + \cos 2\pi\sigma \frac{\delta}{f} y' \right), \end{aligned} \quad (10)$$

where $\sigma = 1/\lambda$ is the frequency in wave numbers. For polychromatic light one integrates over the spectral density $B(\sigma)$ so that the total intensity distribution at the detector becomes

$$I(\mathbf{r}') = 1/2 \int_0^\infty I_0(\mathbf{r}') \left(1 + \cos 2\pi\sigma \frac{\delta}{f} y' \right) B(\sigma) d\sigma. \quad (11)$$

The intensity distribution in the image plane is modulated by the cosine function with the period depending on the wavelength, completely analogous to the scanning interferometer result.³¹ The only distinction is a scaling factor δ/f for the optical path difference in Eq. (11).

This general treatment provides a theoretical basis for the new hybrid imaging and spectral mode of HFTS operation, realized in the high-etendue imaging FTS.^{32,33} According to Eq. (11), for an infinitely distant object the HFTS will produce its image at the detector modulated by the static interference pattern. By tilting the instrument (or by moving the object), we can measure the whole interferogram for each point of the object, providing both imaging and spectral information.

B. Some Theoretical Limits of Holographic Fourier-Transform Spectrometer Performance

The eikonal of Eq. (8) is precise and not a paraxial approximation. Since there is no field coordinate dependence in Eq. (10), an extremely large theoretical throughput is possible for a HFTS with ideal Fourier optics. Hence the HFTS can be even more effective than the scanning FTS for which there exists a restriction on the resolving power, namely, $R = \sigma/\delta\sigma$: $R\Xi \leq 2\pi$,³¹ where Ξ is a solid angle subtended by the object from the entrance pupil. Here the entrance pupil is the Fourier lens in Fig. 1.

1. Resolution and Spectral Range

To find the resolving power of the HFTS, let the intensity distribution from Eq. (11) be sampled by an array detector with a pitch h and N elements along the Y' axis. This corresponds to a step $(\delta/f)h$ in the optical path difference so that the maximum non-aliased wave number is

$$\sigma_{\max} = f/(2h\delta). \quad (12)$$

For a double-sided interferogram the maximum optical path difference L becomes

$$L = 0.5Nh\delta/f = 0.5D\delta/f = 0.5n'\delta/F, \quad (13)$$

where Nh , the array length, should be made equal to the effective Fourier lens diameter D and where $F = f/D$ is the F -number of the Fourier lens. Hence the maximum path difference achievable is directly proportional to the shift δ in the interferometer and is inversely proportional to the F -number of the Fourier optics. The resolution (FWHM) is

$$\delta\sigma = 0.602/L = 1.204f/(Nh\delta) = 1.204F/(n'\delta), \quad (14)$$

so the resolving power becomes

$$R = N/2.408. \quad (15)$$

The equations for a single-sided interferogram are referenced below for future use:

$$L = Nh\delta/f = D\delta/f = n'\delta/F, \quad (13')$$

$$\delta\sigma = 0.602/L = 0.602f/(Nh\delta) = 0.602F/(n'\delta), \quad (14')$$

$$R = N/1.204. \quad (15')$$

2. Signal-to-Noise Ratio

The noise analysis of Fourier spectrometers, including the HFTS, has already been published in several papers and books.^{24,34-39} Here this subject is reexamined in the context of miniaturization. High-quality array detectors for the visible spectral range usually have dark current and readout noise much less than the photon shot noise. But for a miniature room-temperature device, noisier uncooled detectors (because of size and power limitations) are expected. The result is that the shot noise is of less importance than the detector noise. Since this is also true in the infrared, both spectral regimes can now be considered together.

To find the relation between the noise in the interferogram and in the spectrum, the single-sided interferogram is used in Eq. (11). The definitions are $0.5I_0(r') = \text{const} = I_0$, $(\delta/f)y' \equiv u$, and for the variable part

$$I(u) = I_0 \int_0^\infty B(\sigma) \cos 2\pi\sigma u d\sigma. \quad (16)$$

Let $\kappa = 2\pi\sigma$, then the cosine transformation⁴⁰ becomes

$$\sqrt{8\pi}I(u)/I_0 = \sqrt{2/\pi} \int_0^\infty B(\kappa/2\pi) \cos \kappa u d\kappa. \quad (17)$$

The inverse transform yields^{35,36}

$$B(\sigma) = 4 \int_0^\infty [I(u)/I_0] \cos 2\pi\sigma u du. \quad (18)$$

The introduction of an additive noise contribution can be written as

$$B(\sigma) + \Delta B = 4 \int_0^\infty [I(v)/I_0 + \Delta I/I_0] \cos 2\pi\sigma v dv. \quad (19)$$

Using Eq. (18) produces

$$\Delta B(\sigma) = 4 \int_0^\infty [\Delta I(u)/I_0] \cos 2\pi\sigma u du. \quad (20)$$

Applying Parseval's identity yields

$$1/4 \int_0^\infty [\Delta B(\sigma)]^2 d\sigma = \int_0^\infty [\Delta I(u)/I_0]^2 du. \quad (21)$$

Introducing averages in spectral and spatial domains yields from Eq. (21)

$$\overline{\Delta B^2} \sigma_{\max} = 4L \overline{\Delta I^2} / I_0^2, \quad (22)$$

or, defining $\varepsilon_\sigma^2 \equiv \overline{\Delta B^2}$ and $\varepsilon_u^2 \equiv \overline{\Delta I^2} / I_0^2$, the relation becomes

$$\varepsilon_\sigma = 2\varepsilon_u \sqrt{L/\sigma_{\max}}. \quad (23)$$

According to Ref. 39 the signal-to-noise ratio in the interferogram can be defined as

$$(S/N)_u \equiv [I(0)/I_0] / \varepsilon_u. \quad (24)$$

Substituting Eq. (16) with $u = 0$ into Eq. (24) and using Eqs. (23), (12), and (13'), we obtain

$$\begin{aligned} (S/N)_u &= \bar{B} \sigma_{\max} / (0.5\varepsilon_\sigma \sqrt{\sigma_{\max}/L}) \\ &= (S/N)_\sigma 2 \sqrt{\sigma_{\max} L} \\ &= (S/N)_\sigma \sqrt{2N}, \end{aligned} \quad (25)$$

where $\bar{B} \equiv (1/\sigma_{\max}) \int_0^\infty B(\sigma) d\sigma$. The signal-to-noise ratio in the spectral domain is defined by the ratio $(S/N)_\sigma \equiv \bar{B}/\varepsilon_\sigma$ of the average spectral density and the root-mean-square noise. Equation (25) is valid for both a scanning FTS and a static HFTS and illustrates how the signal-to-noise ratio in the spectral domain can be found given its value in the spatial domain. Further noise analysis requires certain assumptions regarding the nature of the noise, so the two cases of dominant detector noise and of dominant photon shot noise are treated separately.

Detector dark noise. The detector noise is proportional to the square roots of the pixel area and the accumulation time T so that

$$\varepsilon_u = \varepsilon_u^0 \sqrt{hHT}, \quad (26)$$

where H is the detector element height. The radiation falling on the array is sampled by N detectors, so the signal accumulated for time T at the zero path difference pixel is

$$I(0)/I_0 = \Lambda(A\Omega)_{\text{HFT}} T/N, \quad (27)$$

where Λ is proportional to the radiance of the object, A is the object area, and Ω is the solid angle sub-

tended by the entrance pupil. The product $(A\Omega)_{\text{HFT}}$ is the throughput of the HFTS (or etendue, see Ref. 31, p. 21). Substituting Eqs. (27) and (26) into Eqs. (24) and (25) yields

$$\begin{aligned} (S/N)^{\text{HFT}} &= \Lambda(A\Omega)_{\text{HFT}} \sqrt{T} / (\epsilon_u^0 N \sqrt{2NhH}) \\ &= \Lambda(A\Omega)_{\text{HFT}} \sqrt{T} / (\epsilon_u^0 N \sqrt{2\Sigma}), \end{aligned} \quad (28)$$

where $\Sigma = NhH$ is the array detector total area. It is instructive to compare Eq. (28) with the signal-to-noise ratio expected for dispersive instruments, both multichannel and scanning.

For a multichannel spectrograph with the same array detector and the same object,

$$\begin{aligned} (S/N)^{\text{MD}} &= \Lambda(A\Omega)_D \sqrt{T} / (N\epsilon_u^0 \sqrt{hH}) \\ &= \Lambda(A\Omega)_D \sqrt{T} / (\epsilon_u^0 \sqrt{N\Sigma}), \end{aligned} \quad (29)$$

where $(A\Omega)_D$ is the throughput of the dispersive instrument, with the same meaning for the parameters A and Ω .

For a scanning dispersive spectrometer the detector is taken to be a single pixel of the array. The accumulation time at each spectral component will be N times less than in the multichannel spectrograph given the same total measurement time, so the signal-to-noise ratio is

$$\begin{aligned} (S/N)^{\text{SD}} &= \Lambda(A\Omega)_D \sqrt{T/N} / (N\epsilon_u^0 \sqrt{hH}) \\ &= \Lambda(A\Omega)_D \sqrt{T} / (\epsilon_u^0 N \sqrt{\Sigma}). \end{aligned} \quad (30)$$

Source shot noise. The photon shot noise with Poisson statistics is given by the square root of the number of detected photons. Assuming that the signal is proportional to the number of photons and by use of Eq. (27), the interferogram signal-to-noise ratio is

$$(S/N)_u^{\text{HFT}} = [\Lambda(A\Omega)_{\text{HFT}} T/N]^{1/2}. \quad (31)$$

In the spectral domain it becomes

$$(S/N)^{\text{HFT}} = [\Lambda(A\Omega)_{\text{HFT}} T]^{1/2} / (\sqrt{2}N) \quad (28')$$

For shot noise, Eqs. (29) and (30) for dispersive spectrometers become

$$(S/N)^{\text{MD}} = [\Lambda(A\Omega)_D T]^{1/2} / \sqrt{N}, \quad (29')$$

$$(S/N)^{\text{SD}} = [\Lambda(A\Omega)_D T]^{1/2} / N. \quad (30')$$

Signal-to-noise ratio and miniaturization limits. The signal-to-noise ratio is an important parameter for the determination of the miniaturization limit; however, so far the relations derived above enable us to draw few conclusions. Generally, the resolving power is determined by a particular spectroscopic application, so the number of spectral channels is more or less fixed, see Eqs. (15) and (15'). According to Eqs. (28)–(30), detector-dominated noise favors a smaller pixel size and a smaller overall detector size for both HFTSs and dispersive multichannel instruments. This is valid only if a high throughput can be

achieved in a small device. (The miniaturization of the spectrometer is not of prime importance for the broad class of remote sensing applications that require a large telescope for good throughput.)

However, for small objects at finite distances, a miniature spectrometer can be optimized in size and a HFTS offers the largest potential in this respect. This advantage is related to the rather limited value of the parameter Ω of the collection optics and a widened field of view for a HFTS compared with a dispersive spectrometer. Comparing the signal-to-noise ratios in Eqs. (28) and (29) yields

$$\begin{aligned} (S/N)^{\text{HFT}} / (S/N)^{\text{MD}} &= (2N)^{-1/2} [(\Lambda\Omega)_{\text{HFT}} / (\Lambda\Omega)_D] \\ &\quad \times (\Sigma^{\text{MD}} / \Sigma^{\text{HFT}})^{1/2}, \end{aligned} \quad (32)$$

where the square root of the detector area ratio $\Sigma^{\text{MD}} / \Sigma^{\text{HFT}}$ gives the characteristic linear scale of the devices.

In general the throughput $A\Omega$ is approximately 200 times larger for a scanning FTS compared with a grating spectrometer (see Ref. 31, p. 22), and for a HFTS the throughput can be even larger. Consider the case of an object of a fixed size (a bacterium spore, for example). The largest achievable numerical aperture of the objective (~ 1.25) together with the object size set the limit of the throughput. According to Eq. (32) the device with a smaller detector will have a higher performance, apart from the factor $(2N)^{-1/2}$. Note that the detector size for a dispersive instrument is dictated by the size of the entrance slit (which is usually the same as a single pixel), but for a HFTS the pixel size can be as small as technically possible. Given both the object and the detector on a microscopic scale, one is tempted to make the whole device on the same scale, possibly incorporated on a silicon chip. But the Lagrange invariant for a fixed throughput determines the product of an angular field of view and the pupil radius. Thus the device with a larger angular field of view can be made smaller, and it was already shown above that the HFTS is restricted only by optical aberrations for this parameter so an aberration analysis is crucial to identify the miniaturization limits of the device.

From this comparison it follows that a sufficiently small HFTS will outperform the corresponding dispersive multichannel spectrograph. For example, for $N = 50$, the HFTS with the same throughput as the dispersive multichannel spectrograph will still have a better signal-to-noise ratio even if its size is ten times smaller. It is miniaturization that brings out this difference.

For the photon shot-noise limit there is no apparent performance gain by making the spectrometer small, as can be seen by Eqs. (28')–(30'). However, the object area A , the only parameter related to the size, restricts the maximum throughput achievable with a dispersive spectrometer and dictates the smallest possible size of the device. The restrictions on the size for HFTSs are much less stringent, and if fast collection optics (large Ω in the throughput relation) are used, it can either be made much smaller

than other types of spectrometer or achieve orders of magnitude higher throughput. In many situations this gain may outweigh even the multiplex disadvantage factor $(2N)^{-1/2}$ in comparison with the multichannel dispersive spectrograph.

The condition for the HFTS to outperform the multichannel spectrograph is found when we divide Eq. (28') by Eq. (29'), yielding

$$(S/N)^{\text{HFT}}/(S/N)^M = (2N)^{-1/2}[(A\Omega)_H/(A\Omega)_D]^{1/2} > 1,$$

$$(A\Omega)_H/(A\Omega)_D > 2N. \quad (33)$$

Again, as in Eq. (32) there is the multiplex disadvantage factor $(2N)^{-1/2}$, and it is harder for HFTSs to compete with the multichannel dispersive spectrometer. For the example with $N = 50$ considered above, the HFTS comes out on top only if its throughput is 100 times better.

3. Experimental Realization of a Miniature Holographic Fourier-Transform Spectrometer

With commercially available off-the-shelf components, an interferometer of high quality has been fabricated and assembled into a complete spectrometer with a complementary metal-oxide semiconductor array detector and a laptop computer. In subsections 3.A–3.C we describe this device in detail.

A. Construction

An asymmetric Sagnac interferometer was made from two Littrow BK7 glass prisms as shown in Fig. 2. The beam splitter was produced with a 45-Å chromium film deposited on one half of the hypotenuse of one of them. To introduce the displacement d of the Sagnac interferometer mirror, the prisms are shifted along the hypotenuse (see Fig. 2). The size of the interferometer was determined by the smallest commercially available Littrow prism, it had a short leg of 12.7 mm. Custom optical shop processing was required for standard 6-mm-diameter lenses with an effective focal length 15 mm. The lens thickness was reduced to match the positions of the focal points inside the interferometer, however, because index-matching glue was used, the precision and the surface quality had much larger tolerances than for other important surfaces. A three-dimensional picture of the Littrow prism HFTS is shown in Fig. 3.

To avoid tilts in the interference pattern and to set the shift d at the design value, the following procedure was used at the assembly stage. The two Littrow prisms were mounted on precise positioning stages, providing a complete six-dimensional control of their mutual positions (X , Y , Z , and three rotational axes), and the He–Ne laser fringe orientation and spacing was monitored in real time. By use of a UV-curable glue, the correct orientation of the prisms was easily fixed.

A complete spectral device included on-line numerical processing of the spectra with a laptop computer. A custom-made Delrin case held the interferometer and a 45° mirror, directing the output beam at the

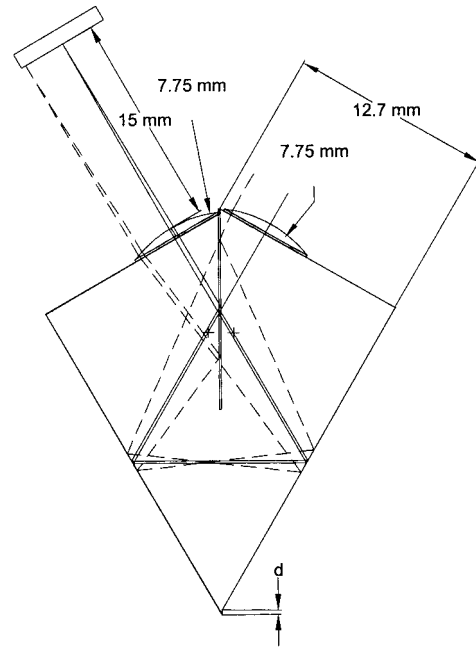


Fig. 2. Ray tracing for a HFTS made from standard microlenses and Littrow prisms. Asymmetry in the interferometer is introduced when one of the prisms is shifted by the distance d along the hypotenuse.

detector. The spectrometer also included a board-level camera PixeLINK PL-A633 from Vitana Corp. with 1280×1024 active pixels ($7.5 \mu\text{m} \times 7.5 \mu\text{m}$ each).

B. Operation

In this instrument two identical lenses are used in the infinite conjugate arrangement, resulting in the cancellation of aberration coefficients for odd powers of the field coordinate. The intermediate virtual images of the source are formed exactly at the Littrow prism hypotenuse, equal distances from both lenses.

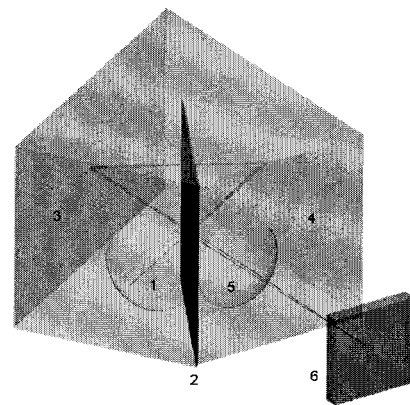


Fig. 3. Three-dimensional picture of the Littrow prism HFTS. The light from an infinite source is focused by the entrance lens 1 into the asymmetric Sagnac interferometer formed by beam splitter 2 and mirrors 3 and 4. The lens 5 collimates the exiting beams and overlaps them at detector 6.

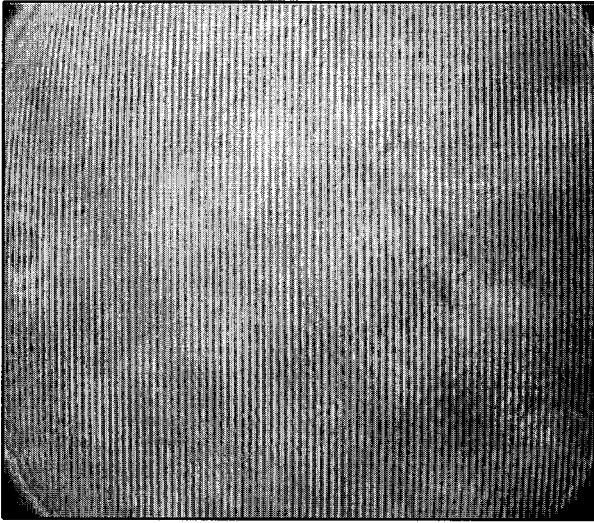


Fig. 4. Interference pattern produced in the Littrow prism HFTS by a He-Ne laser. Speckles are almost absent because of the high quality of the standard optical parts used in the interferometer.

A numerical aperture of 0.2 is large enough for investigation of the aberration effects on the performance of the spectrometer.

In the computer-controlled instrument the interference pattern is digitized with a 1.3-megapixel complementary metal-oxide semiconductor sensor and is sent to the laptop computer equipped with an IEEE-1394 port. The software written in LabVIEW uses the standard API library, provided by the sensor manufacturer. Operating parameters, including in particular the exposure time, size of the subwindow, and gain can be controlled through the software. All digital processing, although not optimized for speed, typically takes less than 200 ms, including the real-time display of the spectral information at the computer monitor. The speed is dominated by the time required to send the frame from the sensor to the computer.

C. Testing

To test the quality of the interferometer, an interference pattern from a He-Ne laser was recorded. It is shown in Fig. 4. Speckles are almost absent because of the high quality of the standard optical components. The performance of the computer-controlled spectrometer is illustrated in Figs. 5 and 6. The interferogram for a neon lamp source is shown in Fig. 5. The asymmetric intensity distribution in the interferogram results from the incidence angle dependence of the effectiveness of the beam splitter. The resulting neon spectrum is shown in Fig. 6. Low resolution resulting in smearing of many sharp emission lines makes it difficult to compare this spectrum with the data in the literature. To demonstrate the broad range of the device, a spectrum of the UV LED emitting at 370 nm is also represented by the dotted curve. Because of the lower sensitivity of the detector in the UV region, the LED spectrum was multi-

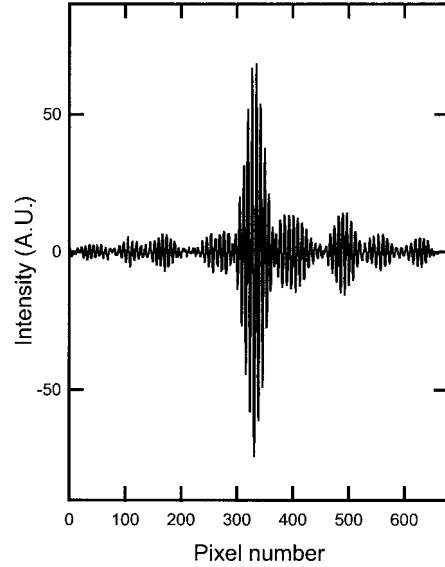


Fig. 5. Interferogram of the neon lamp measured with the Littrow prism HFTS. Intensity nonuniformities are removed.

plied by a factor of 15. As can be seen from the example, a UV-visible-near-IR spectral coverage is easily achieved with HFTS made from simple, inexpensive, and readily available optical and electronic components.

Nonuniformities in the dark current of the detector pixels degrade the signal-to-noise ratio obtained in the spectrum and are a source of spectral artifacts because of the periodic distribution of the defects. Nevertheless, by subtraction of the dark current contribution the values of the lowest detectable signals are decreased dramatically. For example, the max-

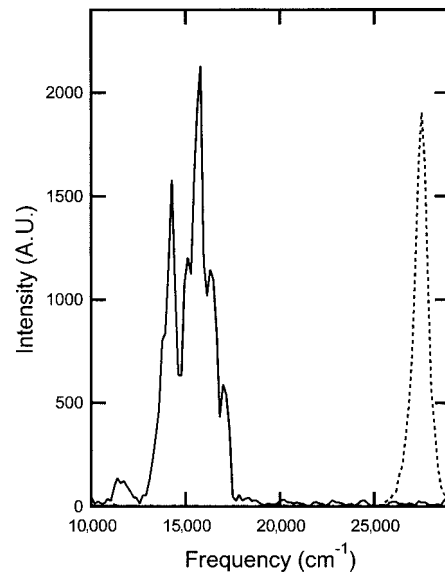


Fig. 6. Spectrum of the neon lamp calculated from the interferogram in Fig. 5 (solid curve). Spectrum of the UV LED emitting at 370 nm (dotted curve, multiplied by 15) demonstrates the wide spectral range of the spectrometer.

imum value in the spectrum in Fig. 6 is ~ 2000 units, which is 5 orders of magnitude larger than the typical noise fluctuations of 0.02 units achieved in the spectra with the dark current removed.

The resolution achieved by the spectrometer was $\delta\sigma = 260 \pm 30 \text{ cm}^{-1}$ for a theoretical limiting value of 204 cm^{-1} . A significant deviation from ideal performance was found in spectra from extended sources. For an angular size of the source in the interferometer plane exceeding 2° , the interference contrast rapidly decreases, resulting in a significant deterioration of the throughput. Nevertheless, in the vertical direction the acceptance angle is much larger (at least 10°) with its value determined essentially by means of vignetting at the Fourier lens.

There is some value in comparing the throughput achieved in this HFTS with that of a typical commercial miniature dispersive spectrograph. We assume that the spectrograph has a fiber input with the radius $r = 25 \text{ }\mu\text{m}$ and $F/4$ optics—these are parameters used in instruments with a resolving power of ≈ 100 , similar to what was demonstrated with our miniature HFTS. The throughput can then be calculated either as a product of the source area and the solid angle subtended by the entrance pupil or as a product of the entrance pupil area and the solid angle subtended by the object—both definitions produce the same result. For the dispersive spectrometer, one finds $(A\Omega)_D = \pi^2 r^2 (1/F/\text{number})^2/4 = 9.6 \times 10^{-5} \text{ mm}^2$, whereas for the Littrow prism HFTS, $(A\Omega)_{\text{HFT}} = (\pi D^2/4)(\pi\alpha^2/4) = 2.7 \times 10^{-2} \text{ mm}^2$, where $D = 6 \text{ mm}$ is the input lens diameter and $\alpha = 0.035 \text{ rad}$ is the acceptance angle. The ratio $(A\Omega)_{\text{HFT}}/(A\Omega)_D = 280$ and it is actually larger than the value $2N = 200$ at which, according to Eq. (33), the HFTS will outperform the multichannel spectrograph. In the detector noise case (i.e., for weak signals) the condition of Eq. (32) is even easier to meet. Namely, for the same detector area the throughput ratio should exceed a factor $2N = 14$, which is much less than the demonstrated experimental value of 280.

4. Effects of Aberrations on the Performance of the Holographic Fourier-Transform Spectrometer

For a miniature HFTS without external optics there is little freedom in the choice of optical design solutions. It is impractical to resort to complex lens designs involving many spherical surfaces in a device of only few millimeters (or micrometers) in size. Proper analysis of aberration effects is a necessary condition to optimize a miniature HFTS and as well as for the incorporation of aspheric surfaces into its design. It is anticipated that a HFTS instrument at the millimeter length scale will be made in this way because of the modern state of glass molding and microlens shaping techniques. In the following we consider this question theoretically and use the results in the analysis of the Littrow prism HFTS. The effects produced by monochromatic and chromatic aberrations are treated separately.

This general analysis of aberrations in a HFTS is based on the approximate axial symmetry and a lin-

ear expansion of the point eikonal function valid for small values of the shearing parameter δ/f : In a previous analysis of aberrations in a HFTS, only the spread of the shear angle was considered.⁴¹

A. Monochromatic Aberrations Theory

To account for nonideal Fourier optics, the term in square brackets in Eq. (7) is expanded with respect to the shearing parameter to give

$$\begin{aligned} & \exp ikS(\mathbf{r} - \delta/2, \mathbf{r}') + \exp ikS(\mathbf{r} + \delta/2, \mathbf{r}') \\ &= \exp ikS(\mathbf{r}, \mathbf{r}') \left[\exp\left(-ik \frac{\delta}{2} \frac{\partial S}{\partial y}\right) \right. \\ & \quad \left. + \exp\left(ik \frac{\delta}{2} \frac{\partial S}{\partial y}\right) \right] \\ &= \exp ikS(\mathbf{r}, \mathbf{r}') 2 \cos\left(2\pi\sigma \frac{\delta}{2} \frac{\partial S}{\partial y}\right). \end{aligned} \quad (34)$$

Here the shearing in the interferometer occurs along the Y axis as illustrated in Fig. 1. Substituting Eq. (34) into Eq. (7) and then into Eq. (6) yields

$$I(\mathbf{r}') = \int |K_p(\mathbf{r}, \mathbf{r}')|^2 0.5 \left(1 + \cos 2\pi\sigma \delta \frac{\partial S}{\partial y}\right) I(\mathbf{r}) d^2\mathbf{r}. \quad (35)$$

In contrast to Eq. (10) the cosine term under the integral can depend on the field coordinates \mathbf{r} and cannot be factored out. We can realize the physical meaning of this fact by noting that $\partial S/\partial y = -n\mathcal{L}$ (see Ref. 30, p. 23), where \mathcal{L} is the direction cosine along the Y axis in the object plane. The dependence of the direction cosine on the field coordinate \mathbf{r} occurs because the rays that come to the same point \mathbf{r}' in the back focal plane have different values of the direction cosine in the object space, or, equivalently, that the rays with the same value of the direction cosines but originating from different points in the field do not come to the same point at the back focal plane. In the following we consider the intensity distribution at the detector due to the point source at an arbitrary position \mathbf{r} in the field of view.

To obtain a quantitative representation for $\partial S/\partial y$, we assume that the rotational symmetry is approximately preserved because of the small value of the shearing parameter δ/f , so the point eikonal S can be expanded in the Taylor series in axially symmetric terms (in analogy to the expansion of the angle eikonal used in some optical systems as described in Ref. 30, p. 255). With terms up to the fourth order in the field and pupil coordinates, the approximate eikonal, now called S_4 , can be written as

$$\begin{aligned} S_4 = & a_{100}K + a_{010}P + a_{001}T + a_{200}K^2 + a_{020}P^2 \\ & + a_{002}T^2 + a_{110}KP + a_{011}PT + a_{101}KT. \end{aligned} \quad (36)$$

This expression is exact for the primary aberration terms. The spherically symmetric coordinates

$$K = 1/2(\xi^2 + \eta^2), P = \xi\xi_P + \eta\eta_P, T = 1/2(\xi_P^2 + \eta_P^2) \quad (37)$$

are expressed in dimensionless coordinates with the pupil location chosen at the detector plane:

$$\xi = y/f, \eta = x/f, \xi_P = y'/f, \eta_P = x'/f. \quad (38)$$

We assume that the aberration content of lenses preceding the Fourier lens is also included in Eq. (36). The field derivative of the expanded eikonal can be found with the aid of the following relation:

$$f \frac{\partial S}{\partial y} = \frac{\partial S}{\partial \xi} = \frac{\partial S}{\partial K} \frac{\partial K}{\partial \xi} + \frac{\partial S}{\partial P} \frac{\partial P}{\partial \xi} = \frac{\partial S}{\partial K} \xi + \frac{\partial S}{\partial P} \xi_P, \quad (39)$$

where Eqs. (37) and (38) were used. From Eq. (39) and Eq. (36) we have

$$f \frac{\partial S_4}{\partial y} = a_{100}\xi + a_{010}\xi_P + a_{200}2K\xi + a_{020}2P\xi_P + a_{110}(P\xi + K\xi_P) + a_{011}T\xi_P + a_{101}T\xi. \quad (40)$$

The product of the eikonal derivative and the focal length f in Eq. (40) gives the value, which is directly comparable to the pupil coordinates \mathbf{r}' . It can be shown also that in the absence of a defocus the coefficient $a_{100} = 0$, and from Eq. (8) it follows that $a_{010} = -f$ and the other terms then give the shift with respect to the ideal, aberration-free position in the interference pattern in the detector plane. Another interesting observation is that the spherical aberration term $a_{002}T^2$ in Eq. (36) disappears after differentiation. This fact illustrates the difference from imaging optics and emphasizes the importance of a detailed aberration analysis in the design of a HFTS.

B. Monochromatic Aberrations Experiment

To reveal experimentally the role of various aberrations, the interference pattern in the detector plane was carefully analyzed. The exact positions of the He-Ne laser fringes were determined in the Littrow prism HFTS both at the center region of the interference pattern and at the side of the pattern as a function of the field angle α , related in the paraxial approximation to the normalized field coordinate ξ of the output Fourier lens in a simple way, $\xi = \alpha$. The two cases correspond to the following conditions: (1) $\eta = \eta_P = \xi_P = 0$ and (2) $\eta = \eta_P = 0, \xi_P \neq 0$. Equation (40) can then be simplified for (1) and (2) sets of the coordinates, respectively:

$$f \frac{\partial S_4}{\partial y} = a_{100}\xi + a_{200}\xi^3, \quad (41)$$

$$f \frac{\partial S_4}{\partial y} = -f\xi_P + 1/2a_{011}\xi_P^3 + [\alpha_{100} + (2a_{020} + 1/2a_{101})\xi_P^2]\xi + 3/2a_{101}\xi_P\xi^2 + a_{200}\xi^3.$$

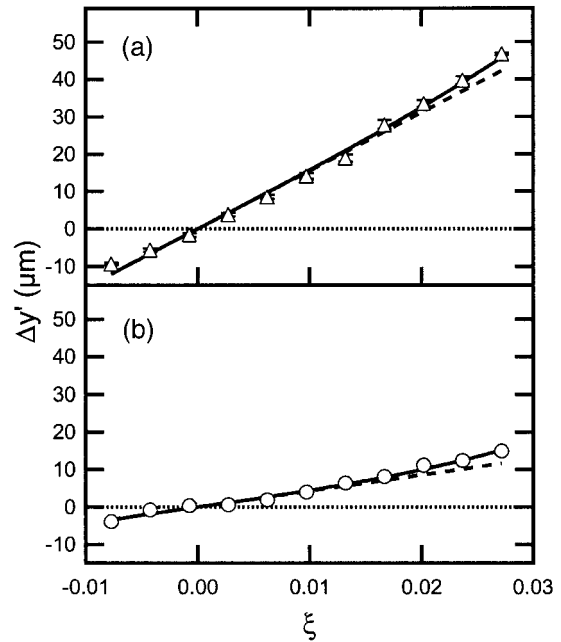


Fig. 7. Shifts of the He-Ne laser fringes in the Littrow prism HFTS versus the normalized field coordinate ξ for two pupil positions: (a) at $\xi_P = 0.1, \eta_P = 0$; (b) at $\xi_P = \eta_P = 0$. The solid curve shows the fit of the experimental values with only primary aberrations taken into account. The dotted lines represent contributions from aberrations with linear field dependence.

The measured positions of the fringes for $\xi_P = 0.1$ and $\xi_P = 0$ are shown in Figs. 7(a) and 7(b) correspondingly (the term $-f\xi_P$ is removed to emphasize the aberration effects). We obtain the coefficients a_{100} and a_{200} by fitting the data in Fig. 7(b) with first formula of Eqs. (41), plus an arbitrary constant term. We achieve fine-tuning of the field zero position by matching the constant terms for cases (1) and (2). Zero values for the coma (a_{011}) and the distortion (a_{110}) aberration coefficients are assumed because of the symmetric optical arrangement. The value of the coefficient a_{200} , describing the pupil spherical aberration, is then kept fixed (since the corresponding term does not depend on the pupil coordinate ξ_P) while the data are fitted in Fig. 7(b) with the second formula of Eqs. (41). From the two fits the primary aberration coefficients can be estimated. Their values are presented in Table 1.

The linear field terms, shown with dotted lines in Figs. 7(a) and 7(b) dominate over the cubic contribution for values of the field coordinate $\xi < 0.03$. In the axial region of the pupil this term is due to the defocusing ($a_{100}\xi$), and in the marginal region $\xi_P = 0.1$ an additional contribution from astigmatism and field curvature $[(2a_{020} + 1/2a_{101})\xi_P^2\xi]$ is two times larger. With the laser fringe width of $\sim 60 \mu\text{m}$, the phase shift exceeds half of a wavelength for $\xi > 0.02$ at $\xi_P = 0.1$, resulting in smearing out of the interference pattern in the marginal region; broadening of the spectral lines; and, as a consequence, in reduction of the throughput.

In the case of noncompensated coma, the term α_{011}

Table 1. Values of Primary Aberration Coefficients

ξ_P	a_{100} (mm)	α_{200} (mm)		a_{011} (mm)	$2a_{020} + 1/2a_{101}$ (mm)		a_{110} (mm)
		Experiment	Calculation		Experiment	Calculation	
0	0.43 ± 0.04	170 ± 70	132	0	—	—	0
0.1	—	—	—	0	110 ± 6	178	0

$T \xi_P = 1/2a_{011} (\xi_P^2 + \eta_P^2)\xi_P$ in Eq. (40) results in the fringe period monotonically changing with the pupil meridional and saggital positions even in the case of small values of the field coordinates ξ and η . It results in the deterioration of the spectral resolution and the asymmetric shape of the instrument function.

There is a direct correspondence between the primary wave-front aberrations and the point eikonal aberrations in the case of a Fourier lens. It follows from the fact that the ideal Fourier lens transforms the light emitted from any point in the object plane into a plane wave in the image space. In the paraxial approximation any deviations from the ideal eikonal function of Eq. (8) will be equal to the wave-front error at the back focal position of the lens. By using this fact, we can base the optimization in the design of a HFTS on minimization of certain Zeidel aberration coefficients (see Ref. 42, p. 139) available in most optical design software packages. As an illustration, the value of the coefficient ($2a_{020} + 1/2a_{101}$) was calculated from Zeidel aberration coefficients S_{III} (astigmatism) and S_{IV} (Petzval field curvature) according to the relation, derived by comparison with the standard wave-front aberration polynomial⁴³ and Eq. (36):

$$2a_{020} + 1/2a_{101} = 3/2 S_{III} + 1/2 S_{IV}. \quad (42)$$

From OSLO optical design software we have $S_{III} = 0.024$ mm and $S_{IV} = 0.0042$ mm for a Littrow prism HFTS, indicating that the astigmatism is the main aberration affecting the device performance. In Table 1 the experimental and calculated values are shown with the calculation taking into account a different normalization of the field and pupil coordinates in OSLO and in this paper. The value of the coefficient a_{200} is given by the pupil spherical aberration, and its calculated value is also presented in Table 1. It is not surprising that the measured coefficients are quite different from the calculated values, most probably because of the neglect of the higher-order aberrations. But the values are still close enough to justify use of the primary aberrations in the optimization procedure.

C. Chromatic Aberrations

Dispersion of the Fourier lens of a HFTS results in the renormalization of frequencies in the spectrum and in the degradation of the fringe visibility. Both effects are considered here separately.

1. Frequency Shift

Dispersion in the refraction coefficients n and n' is responsible for the wavelength dependence of the focal length of the Fourier lens $f = r/(n - n')$ and for a corresponding change of the coefficient δ/f . They determine the scaling of the interferogram in the detector plane. According to Eq. (10), the intensity at the detector is modulated by factors $\cos 2\pi\sigma_0 (\delta/f_0)y'$ and $\cos 2\pi\sigma(\delta/f)y'$ for wave numbers σ_0 and σ . If one of the frequencies is chosen as a reference (let it be σ_0), then all other frequencies will appear shifted in the spectrum according to the following formula:

$$\sigma_m = \sigma f_0/f = \sigma n_0'(n - n')/[n'(n_0 - n_0')], \quad (43)$$

where σ is the true value of the frequency and σ_m is its measured value. In the miniature HFTS described in this paper, we chose the frequency of the He-Ne laser $\sigma_0 = 15802.37 \text{ cm}^{-1}$ as a reference. The calculated frequency shift $\sigma_m - \sigma$ for the BK7 glass dispersion is shown in Fig. 8 with a solid curve. Experimental values, measured for several mercury emission lines, follow the theoretical curve almost ideally as can be seen from Fig. 8.

2. Fringe Visibility Degradation

Despite the large value of the frequency shift, it is easy to take into account by an appropriate rescaling

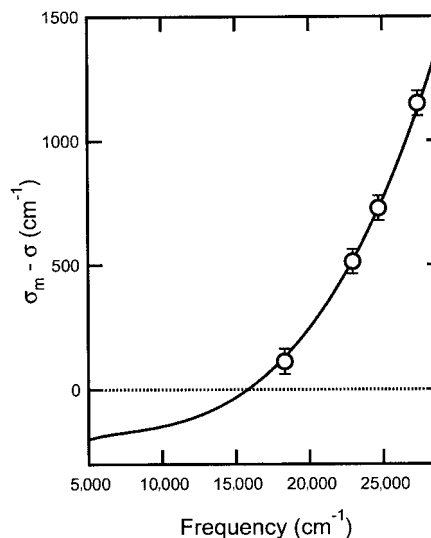


Fig. 8. Frequency shift due to the chromatic aberrations in the HFTS made from BK7 glass. The solid curve is calculated according to Eq. (43). The symbols are experimental values measured for several mercury emission lines.

of the frequencies in the spectrum. Potentially, a more serious problem could be defocusing and the loss of contrast in the interference pattern. For an incoherent source the interference pattern at the detector is observed over a small range of distances from the Fourier lens with the maximum at the focal distance. The longitudinal chromatic aberration changes the optimal distance, resulting in the appearance of the defocus for all wavelengths except one. A measurement of the fringe visibility, as a function of distance at several representative spectral frequencies, should provide a measure of the chromatic aberration tolerance. We can make a simple estimate of such an effect by assuming that the two interfering narrow beams lose the coherence when the distance between them at the detector exceeds the size of the area of coherence ρ . This condition is

$$\begin{aligned} \delta(f - f_0)/f_0 &< \rho, \\ (n - n_0)/(n - 1) &< \rho/\delta, \end{aligned} \quad (44)$$

where we set $n' = 1$. Substituting values corresponding to the He-Ne laser and the UV LED emission lines, the condition of inequalities (44) reads $1.6 < \rho/\lambda$. It is possible to make a simple estimate by use of the van Cittert-Zernike theorem (see Ref. 44, p. 508). According to the theorem for a distant source, the size of the area of coherence is $0.16\lambda/\alpha$ at the entrance pupil. Since the detector is located at the same size exit pupil, it is safe to assume the same area of coherence in the detector plane. With the acceptance angle 2° $\rho/\lambda = 9$, the inequalities of (44) are fix valid. Chromatic aberrations and the partial coherence set the limit on the acceptance angle size $2\alpha < 0.2 = 12^\circ$, which is close to the value achievable with aspheric lenses.

5. Summary

Using the point eikonal formalism in the stationary-phase approximation, we demonstrated that a HFTS is capable of operating in the diffraction limit. The rigorous derivation of the intensity distribution at the HFTS output has provided a theoretical basis for some new unconventional applications of this device.

By considering the size dependence of the signal-to-noise ratio, we have identified the conditions under which a miniature HFTS can outperform a competing multichannel dispersive spectrograph. When detector noise dominates, it is shown that miniaturization helps the HFTS to achieve better characteristics than the multichannel dispersive spectrograph for the same throughput. A large value of the throughput parameter of the HFTS, which can be even larger than for the scanning FTS, is the strong point of this device and can result in a better performance than a multichannel dispersive spectrograph even in the shot-noise case.

The experimental realization of the miniature HFTS has achieved a broad UV-visible-near-IR spectral range and a resolving power of 100 by use of

simple and readily available optical components and standard complementary metal-oxide semiconductor array sensors. The aberration-limited throughput in devices with spherical optics emerged as a main hurdle to better performance. With an acceptance angle of only 2° , the tested HFTS throughput is a factor 280 larger than competing miniature spectrographs with the optical fiber input.

We analyzed the effects of monochromatic aberrations on the characteristics of a HFTS by expanding the point eikonal function assuming approximate axial symmetry. The effects of different types of primary aberration are revealed; and for the Littrow prism HFTS with spherical lenses, it was shown that the astigmatism is the main performance-limiting factor. This analysis enables a better design of the HFTS optics by use of primary aberrations in the optimization procedure.

For longitudinal chromatic aberrations, two main effects were identified. First is a simple and predictable shift of the measured spectral frequencies related to the dispersion of the lens material. Second is the degradation of the throughput because of the partial coherence in the detector plain. Because of this factor, a limiting value of 12° for the acceptance angle is derived.

By use of optimally designed aspheric optics, almost an order-of-magnitude improvement in the throughput can be achieved in a simple miniature HFTS. This represents an advance in the field of miniature spectral devices. Our general relations derived in the stationary-phase approximation are valid even in the diffraction limit and can be used to design microspectrometers integrated on a chip, which can be comparable to the wavelength size.

We are grateful for financial support from the Defense Advanced Research Projects Agency, the U.S. Department of Energy, and the New York State Alliance for Nanomedical Technologies. Use of facilities of the Cornell Center for Material Research is also acknowledged.

References

1. I. P. Petrov and B. N. Grechushnikov, "Photographic method of recording in Fourier spectrometry," *Opt. Spectrosc.* **19**, 82–83 (1965).
2. G. W. Stroke and A. T. Funkhouser, "Fourier transform spectroscopy using holographic imaging without computing and with stationary interferometers," *Phys. Lett.* **16**, 272–274 (1965).
3. K. Yoshihara and A. Kitade, "Holographic spectra using a triangle path interferometer," *Jpn. J. Appl. Phys.* **6**, 116 (1967).
4. K. Kamiya, K. Yoshihara, and K. Okada, "Holographic spectra obtained with a Lloyd's mirror," *Jpn. J. Appl. Phys.* **7**, 1129 (1968).
5. K. Yoshihara, K. Nakashima, and M. Higuchi, "Holographic spectroscopy using a Mach-Zehnder interferometer," *Jpn. J. Appl. Phys.* **15**, 1169–1170 (1976).
6. J. W. Cooley and J. W. Tukey, "An algorithm for machine calculation of complex Fourier series," *Math. Comput.* **19**, 297–301 (1965).
7. P. Fellgett, "A propos de la theorie du spectrometre interferentiel multiplex," *J. Phys. Radium* **19**, 187–191 (1958).

8. J. D. Strong and G. A. Vanasse, "Interferometric spectroscopy in the far infrared," *J. Opt. Soc. Am.* **49**, 844–850 (1959).
9. P. Jacquinet, "New developments in interference spectroscopy," *Rep. Prog. Phys.* **23**, 268–312 (1960).
10. L. Genzel, "Aperiodic and periodic interference modulation for spectrographic purposes," *J. Mol. Spectrosc.* **4**, 241–261 (1960).
11. P. L. Richards, "High-resolution Fourier transform spectroscopy in the far-infrared," *J. Opt. Soc. Am.* **54**, 1474–1484 (1964).
12. I. G. Nolt and A. J. Sievers, "Stress induced frequency shift of a lattice resonant mode," *Phys. Rev. Lett.* **16**, 1103–1105 (1966).
13. H. D. Drew and A. J. Sievers, "Far-infrared absorption in superconducting and normal lead," *Phys. Rev. Lett.* **19**, 697–699 (1967).
14. L. Genzel and K. Sakai, "Interferometry from 1950 to present," *J. Opt. Soc. Am.* **67**, 871–879 (1977).
15. T. Okamoto, S. Kawata, and S. Minami, "Fourier transform spectrometer with a self-scanning photodiode array," *Appl. Opt.* **23**, 269–273 (1984).
16. T. H. Barnes, "Photodiode array Fourier transform spectrometer with improved dynamic range," *Appl. Opt.* **24**, 3702–3706 (1985).
17. L. V. Egorova, I. E. Leshcheva, B. N. Popov, and A. Y. Stroganova, "Static fast response Fourier spectrometer having a linear CCD image forming system," *J. Opt. Technol.* **56**, 220–221 (1989).
18. J. V. Sweedler and M. B. Denton, "Spatially encoded Fourier transform spectroscopy in the ultraviolet to the near infrared," *Appl. Spectrosc.* **43**, 1378–1384 (1989).
19. W. H. Smith and W. V. Schempp, "Digital array scanned interferometers for astronomy," *Exp. Astron.* **1**, 389–405 (1991).
20. M.-L. Junttila, "Stationary Fourier-transform spectrometer," *Appl. Opt.* **31**, 4106–4112 (1992).
21. S. Takahashi, J. S. Ahn, S. Asaka, and T. Kitagawa, "Multichannel Fourier transform spectroscopy using two-dimensional detection of the interferogram and its application to Raman spectroscopy," *Appl. Spectrosc.* **47**, 863–868 (1993).
22. P. G. Lucey, K. Horton, T. Williams, K. Hinck, C. Budney, J. B. Rafert, and T. B. Rusk, "SMIFTS: a cryogenically-cooled spatially-modulated imaging infrared interferometer spectrometer," in *Imaging Spectrometry of the Terrestrial Environment*, G. Vane, ed., Proc. SPIE **1937**, 130–141 (1993).
23. M. J. Padgett, A. R. Harvey, A. J. Duncan, and W. Sibbett, "Single-pulse, Fourier-transform spectrometer having no moving parts," *Appl. Opt.* **33**, 6035–6040 (1994).
24. W. H. Smith, "Digital array scanned interferometer: sensor and results," *Appl. Opt.* **35**, 2902–2909 (1996).
25. M. Hashimoto and H. Hamaguchi, "Construction of a multichannel Fourier transform infrared spectrometer for single-event time-resolved spectroscopy," *Appl. Spectrosc.* **50**, 1030–1033 (1996).
26. B. A. Patterson, J. P. Lenney, W. Sibbett, B. Hirst, N. K. Hedges, and M. J. Padgett, "Detection of benzene and other gases with an open-path, static Fourier-transform UV spectrometer," *Appl. Opt.* **37**, 3172–3175 (1998).
27. J. T. Daly, E. A. Johnson, A. Bodkin, W. A. Stevenson, and D. A. White, "Recent advances in miniaturization of infrared spectrometers," in *Silicon-based Optoelectronics II*, D. J. Robbins and D. C. Houghton, eds., Proc. SPIE **3953**, 70–87 (2000).
28. J. P. Ferguson and S. Schoenfelder, "Micromoulded spectrometers produced by the LIGA process," in *Proceedings of IEEE Colloquium on Microengineering in Optics and Optoelectronics* (Institute of Electrical and Electronics Engineers, London, UK, 1999), pp. 11/11–11/10.
29. H. J. Caulfield, "Spectroscopy," in *Handbook of Optical Holography*, H. J. Caulfield, ed. (Academic, New York, 1979), pp. 587–594.
30. A. Walther, *The Ray and Wave Theory of Lenses*, Cambridge Studies in Modern Optics (Cambridge U. Press, Cambridge, UK, 1995).
31. R. J. Bell, *Introductory Fourier Transform Spectroscopy* (Academic, New York, 1972).
32. R. F. Horton, "Optical design for a high-étendue imaging Fourier transform spectrometer," in *Imaging Spectrometry II*, M. R. Descour and J. M. Mooney, eds., Proc. SPIE **2819**, 300–315 (1996).
33. K. Dohlen, "Interferometric spectrometer for liquid mirror survey telescopes," in *Optical Telescopes of Today and Tomorrow: Following in the Direction of Tycho Brahe*, A. Ardeberg, ed., Proc. SPIE **2871**, 1359–1364 (1996).
34. F. D. Kahn, "The signal: noise ratio of a suggested spectral analyzer," *Astrophys. J.* **129**, 518–521 (1959).
35. M. H. Tai and M. Harwit, "Fourier and Hadamard transform spectrometers: a limited comparison," *Appl. Opt.* **15**, 2664–2666 (1976).
36. R. R. Treffers, "Signal-to-noise ratio in Fourier spectroscopy," *Appl. Opt.* **16**, 3103–3106 (1977).
37. J. Zhao and R. L. McCreery, "Multichannel FT-Raman spectroscopy: noise analysis and performance assesment," *Appl. Spectrosc.* **51**, 1687–1697 (1997).
38. F. M. Reininger, "The application of large format, broadband quantum well infrared photodetector arrays to spatially modulated prism interferometers," *Infrared Phys. Technol.* **42**, 345–362 (2001).
39. S. P. Davis, M. C. Abrams, and J. W. Brault, *Fourier Transform Spectrometry* (Academic, San Diego, Calif., 2001).
40. K. Ito, ed., *Encyclopedic Dictionary of Mathematics*, 2nd ed. (MIT, Cambridge, Mass., 1987), Vol. 2.
41. R. G. Sellar and J. B. Rafert, "Effects of aberrations on spatially modulated Fourier transform spectrometers," *Opt. Eng.* **33**, 3087–3092 (1994).
42. W. T. Welford, *Aberrations of Optical Systems* (Adam Hilger, Bristol, UK, 1986).
43. R. R. Shannon, *The Art and Science of Optical Design* (Cambridge U. Press, Cambridge, UK, 1997).
44. M. Born and E. Wolf, *Principles of Optics*, 2nd ed. (Pergamon, New York, 1964).